Aggregation-Enhanced Thermally Activated Delayed Fluorescence Efficiency for Two-Coordinate Carbene−Metal−Amide Complexes: A QM/MM Study

Shiyun Lin, Qi Ou, Yu Wang, Qian Peng, and Zhigang Shuai*
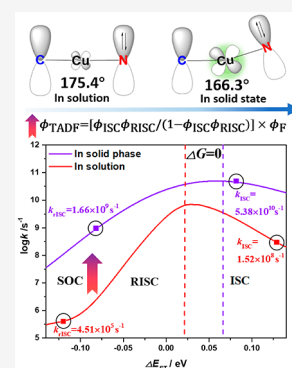
Read Online

ACCESS | Metrics & More | Article Recommendations | SI Supporting Information

ABSTRACT: The two-coordinate carbene−metal−amide complexes have attracted a great deal of attention due to their remarkable thermally activated delayed fluorescence (TADF) properties, giving them promise in organic light-emitting diode application. To reveal the inherent mechanism, we take CAAC−Cu(I)−Cz and CAAC−Au(I)−Cz as examples to investigate the photophysical properties in solution and solid phases by combining quantum mechanics/molecular mechanics approaches for the electronic structure and the thermal vibration correlation function formalism for the excited-state decay rates. We found that both intersystem crossing (ISC) and its reverse (rISC) are enhanced by 2−4 orders of magnitude upon aggregation, leading to highly efficient TADF, because (i) the metal proportion in the frontier molecular orbitals increases, leading to an enhanced spin−orbit coupling strength between S_1 and T_1, and (ii) the reaction barriers for ISC and rISC are much lower in solution than in aggregate phases through a decrease in energy gap ΔE_{ST} and an increase in the relative reorganization energy through bending the angle $\angle C2−Cu−N1$ for T_1. We propose a pump−probe time-resolved infrared spectroscopy study to verify the mechanism. These findings can clarify the ongoing dispute over the understanding of the high TADF quantum efficiency for two-coordinate metal complexes.

The third generation of organic light-emitting diodes (OLEDs) based on thermally activated delayed fluorescence (TADF) molecules has become a mainstream topic of research in organic optoelectronic devices in the past decade.[1−5] A spin statistical limit of 25% under current injection can be overcome through the TADF process, realizing 100% exciton harvesting due to efficient reverse intersystem crossing (rISC) from triplet to singlet states.[6] Great progress has been achieved since Adachi et al. reported high-efficiency TADF-based organic light-emitting diodes (OLEDs) in 2012.[7] Recently, the two-coordinate carbene−metal−amide (CMA) complexes, as shown in Figure 1a, have been demonstrated to have outstanding TADF performance, which has attracted an increasing amount of attention.[8−11] The first groundbreaking work was reported by Di et al.[8] as green electroluminescence (EL) in OLEDs using two-coordinate carbene−gold and carbene−copper complexes with maximum external quantum efficiencies (EQEs) of 26.3% and 9.7%, respectively. Immediately thereafter, Hamze et al.[9] reported a series of two-coordinate Cu(I) complexes as efficient blue-emitting OLED emitters with photoluminescence efficiencies of >99% and microsecond lifetimes.

The understanding of the high-TADF efficiency mechanism for CMA complexes has aroused a broad discussion. Di et al.[8] first claimed that the highly efficient TADF of CMA complexes was caused by the rotationally accessed spin-state inversion (RASI) mechanism, within which the singlet−triplet energy

gap (ΔE_{ST}) can change from positive to negative along the rotational angle between donor and acceptor moieties to realize the barrierless interconversion from triplet to singlet. Soon thereafter, Föller et al.[12] argued that the RASI mechanism was an artifact because the negative ΔE_{ST} was obtained by calculating the S_1 and T_1 states at different quantum chemical levels. They proposed a mechanism based on a fast upconversion process with the coplanar geometry of CAAC−Au(I)−Cz through high-level quantum chemical calculation.[12] Taffet et al.[13] declared that the TADF in CAAC−Cu(I)−Cz was caused by carbene−metal−amide bond deformation rather than the rotation of ligands. In addition, Penfold and co-authors[14−16] have clearly proved the importance of internal rotation for the (r)ISC properties of these complexes by quantum dynamics simulations. Feng et al.[17] explored the CMA luminescence in the solid state through spectroscopic and quantum chemical investigations of the Au-centered molecule, found that the crystalline phase offers well-defined coplanar geometries, and concluded that the more coplanar triplet equilibrium conformations control the photo-
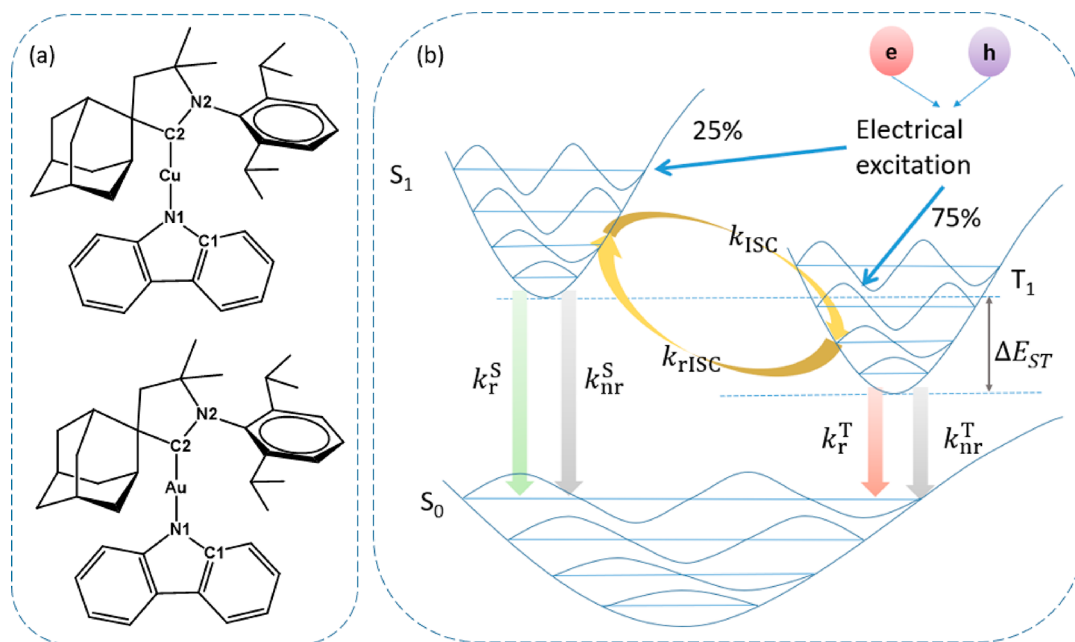
Figure 1. (a) Chemical structures of CAAC−Cu(I)−Cz and CAAC−Au(I)−Cz. (b) Excited-state decay processes for TADF, including radiative (k_r^S) and nonradiative (k_{nr}^S) decay from S_1 to S_0, radiative (k_r^T) and nonradiative (k_{nr}^T) decay from T_1 to S_0, and ISC (k_{ISC}) and rISC (k_{rISC}) between S_1 and T_1.

physics of CMAs. However, the aggregation effect is yet to be determined for (r)ISC, which needs to be explored throughout the whole photophysical process in detail.

In principle, a fast rISC process requires a small singlet−triplet energy gap (ΔE_{ST}),[18] significant spin−orbit coupling (SOC),[19] and a small activation energy[20] between the S_1 and T_1 states. We systematically calculate the rates for the involved radiative, nonradiative, and ISC/rISC processes (shown in Figure 1b) of two CMAs in solution and solid phases, using our self-developed thermal vibration correlation function (TVCF) formalism.[17−19] We found that upon aggregation, more participation of the metal component strengthens the SOC between the S_1 and T_1 states and the bending C−metal−N angle leads to a larger reorganization energy, which rapidly accelerates ISC/rISC by 2−4 orders of magnitude, thus giving rise to a high-efficiency TADF.

The radiative decay rate constant can be obtained from an integration over the emission spectrum: $k_r(T) = \int \sigma_{em}(\omega, T)\, d\omega$, where $\sigma_{em}(\omega, T)$ is from the Fermi golden rule (FGR):

$$\sigma_{em}(\omega, T) = \frac{2\omega^3}{3\pi h c^3} |\mu_{fi}|^2 \int_{-\infty}^{\infty} e^{-i(\omega - \omega_{fi})t} \rho_{em}(t, T)\, dt \quad (1)$$

where μ_{fi} is the electric transition dipole moment between the initial and final electronic states and $\rho_{em}(t, T) = Z_i^{-1}\mathrm{Tr}(e^{i\tau_f \hat{H}_f} e^{i\tau_i \hat{H}_i})$ is the Franck−Condon overlap at temperature T with Z_i being the vibrational partition function for the initial electronic state and $H_{i(f)}$ the vibrational Hamiltonian for the initial (final) electronic state.

According to FGR and the second-order perturbation theory, the general nonradiative decay rate constant can be expressed as

$$k_{f \leftarrow i} \equiv \frac{2\pi}{h} \sum_{v,u} P_{iv} \left| H'_{fu,iv} + \sum_{n,\mu} \frac{H'_{fu,n\mu} H'_{n\mu,iv}}{E_{iv} - E_{n\mu}} \right|^2 \delta(E_{iv} - E_{fu}) \quad (2)$$

where H' denotes the interaction between two different Born−Oppenheimer states, consisting of two contributions as follows:

$$\hat{H}'\Psi_{iv} = \hat{H}^{BO}\Phi_i(\mathbf{r}; \mathbf{Q})\Theta_v(\mathbf{Q}) + \hat{H}^{SO}\Phi_i(\mathbf{r}; \mathbf{Q})\Theta_v(\mathbf{Q}) \quad (3)$$

where $\hat{H}^{BO}$ is the nonadiabatic coupling and $\hat{H}^{SO}$ is the spin−orbit coupling.

The nonradiative rate constant between two electronic states within the same spin manifold can be written on the basis of the first-order perturbation theory as

$$k_{nr} = \frac{1}{h^2} \sum_{kl} R_{kl} \int_{-\infty}^{\infty} dt\, e^{i\omega_{if}t} \rho_{fi,kl}^{ic}(t, T) \quad (4)$$

where $R_{kl} = \langle \Phi_f | \hat{P}_{fk} | \Phi_i \rangle \langle \Phi_i | \hat{P}_{fl} | \Phi_f \rangle$ is the nonadiabatic electronic coupling matrix element between electronic states Φ_f and Φ_i, $P_{l(k)}$ is the nuclear momentum operator for the lth (kth) vibrational normal mode, and $\rho_{fi,kl}^{ic}(t, T) = Z_i^{-1}\mathrm{Tr}(\hat{P}_{fk}e^{-i\tau_f \hat{H}_f}\hat{P}_{fl}e^{-i\tau_i \hat{H}_i})$.

The ISC/rISC rate constants from initial singlet/triplet to triplet/singlet states can be recast as

$$k_{ISC/rISC} \equiv \frac{1}{h^2} |H_{fi}^{SO}|^2 \int_{-\infty}^{+\infty} dt\, e^{i\omega_{if}t} \rho_{fi}^{ISC/rISC}(t, T) \quad (5)$$

where $\rho_{fi}^{ISC/rISC}(t, T)$ is the Franck−Condon overlap between singlet and triplet excited states. The detailed derivation and solution of equations can be found in our previous work.[21−23]

All parameters needed in eqs 1−3 can be obtained by density functional theory (DFT) and time-dependent DFT (TD-DFT) calculations, which are carried out by using the widely used M06 functional[24] and basis set LANL2DZ for the metal atom and 6-31G(d) for non-metal atoms. The equilibrium geometric optimizations and frequency calculations are performed using the restricted DFT method for S_0, TD-DFT for S_1, and unrestricted DFT for T_1. The excitation energies are calculated at the TD-DFT level. The polarizable continuum model (PCM)[25] for chlorobenzene is adopted to
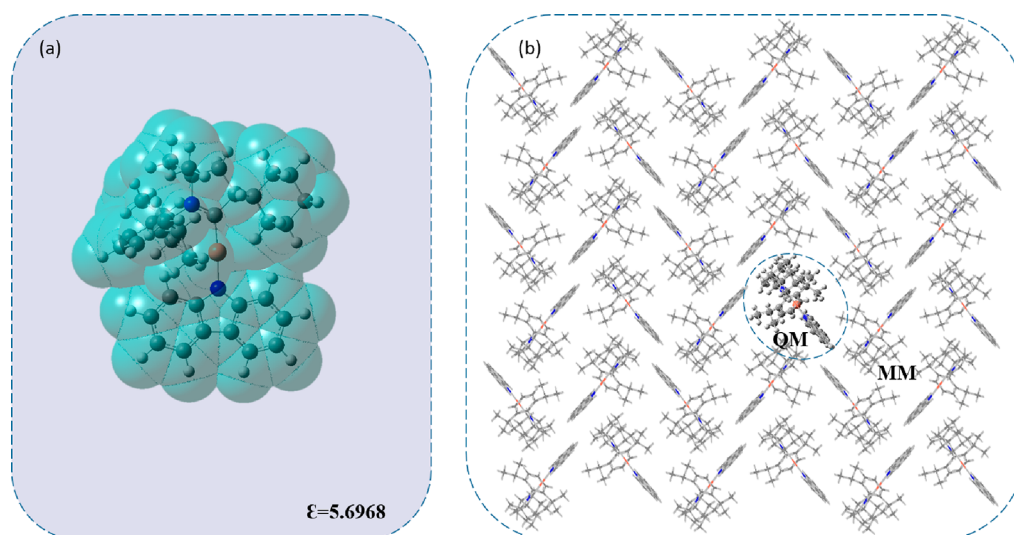
Figure 2. Setup of (a) the PCM and (b) the ONIOM model [taking CAAC−Cu(I)−Cz as an example].
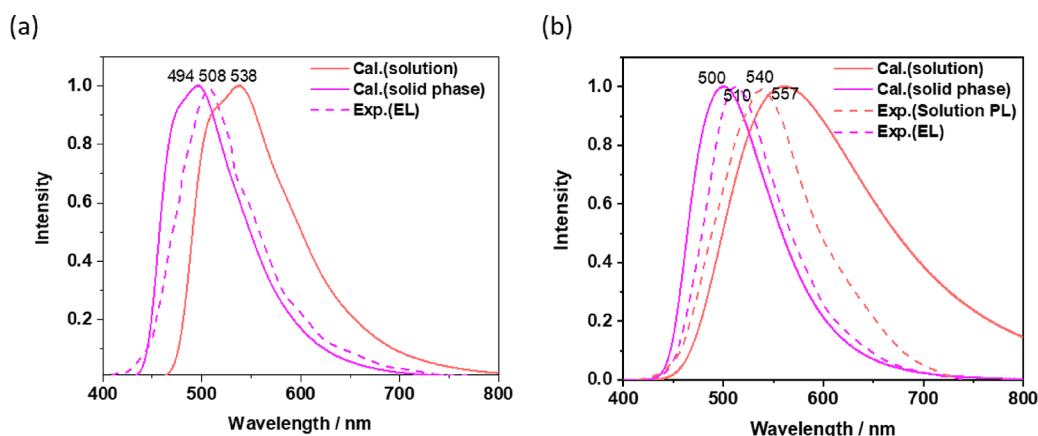

Figure 3. Calculated fluorescence emission spectra (solid line) in chlorobenzene and the solid phase and experimental PL spectra in chlorobenzene and EL spectra (dash line) from the OLED of (a) CAAC−Cu(I)−Cz and (b) CAAC−Au(I)−Cz.

account for the solvent effect (see Figure 2a). To mimic the solid phase environment, the two-layer ONIOM model[26] is constructed by cutting a cluster from the experimental X-ray diffraction (XRD) crystal structure that is 3 × 3 × 3 in size with the central molecule treated using the QM method and the surrounding molecules handled by the efficient universal force field (UFF) method (see Figure 2b). The embedding molecules are kept frozen in their crystal structure orientations with the qeq method and take the polarization effect into consideration to calculate the external point charge. In the QM calculation of the simulated crystal phase, these frozen orientations, along with optimized S_1 coordinates of the embedded molecule, are used. The total size of this simulated crystal phase supercell is 108 molecules (9612 atoms). Executing all-QM excited-state calculations in the quantum chemistry package for such huge system requires many more computational resources than we can practically access. The nonadiabatic couplings are evaluated at the same level in the S_1 optimized geometry. The potential energy surfaces (PESs) are constructed by the relaxed scan along the C−Cu−N coordination bond angle for the excited S_1 and T_1 states. All of these electronic structure calculations are carried out in the Gaussian 16 package.[27] The orbital composition analysis is performed in the Multiwfn package based on the Becke

function.[28] The SOC matrix elements are computed by the one-electron Breit−Pauli Hamiltonian[29] in Q-Chem 5.3[30,31] using the M06 functional and 6-31G(d) for light elements and UGBS for the metal atom in the T_1 optimized geometry with an external point charge to simulate the MM region. The transition dipole moment from T_1 to S_0 is obtained at the M06/6-31G(d)/LANL2DZ level in Dalton with the quadratic response theory.[32] All rate constant calculations are performed with our homemade MOMAP package, which has been successfully applied over a wide range to predict optoelectronic properties in organic light-emitting materials.[26]

The vibrationally resolved emission spectra of S_1 states are calculated for CAAC−Cu(I)−Cz and CAAC−Au(I)−Cz at 298 K in solution and solid phase and plotted in Figure 3, together with the available experimental counterparts for comparison. Figure 3 shows that the emission spectra in aggregates experience a remarkable blue-shift relative to the solution phase. The calculated emission spectra in the solid phase are consistent with the measured EL in terms of both spectral line shapes and peak positions, with very small deviations of 14 nm (0.07 eV) for CAAC−Cu(I)−Cz and 10 nm (0.05 eV) for CAAC−Au(I)−Cz. Such good agreement confirms the reliability for the computational model and methods. This blue-shift originates from the increasing

Table 1. Calculated Rate Constants (s^{-1}) of the Excited-State Decay Processes, TADF Quantum Efficiencies for CAAC−Cu(I)−Cz and CAAC−Au(I)−Cz in a Chlorobenzene Solution and the Solid Phase, and Available Experimental Data

	k_r^S	k_{nr}^S	k_r^T	k_{nr}^T	k_{ISC}	k_{rISC}	$k_{r,avg.}$	ϕ_{TADF} (%)
				CAAC−Cu(I)−Cz				
solution	1.76×10^7	2.51×10^4	2.15×10	1.16×10^4	1.52×10^8	4.51×10^5	6.58×10^4 $(3.0 \times 10^5)^a$	72 $(68)^a$
solid	2.05×10^7	7.07×10^3	1.04×10	1.61×10^4	5.64×10^{10}	1.74×10^9	2.75×10^5	97
				CAAC−Au(I)−Cz				
solution	1.73×10^7	1.86×10^5	2.22×10	5.01×10^3	3.16×10^8	4.48×10^6	2.96×10^4	92
solid	1.67×10^7	2.82×10^4	5.93×10^2	6.16×10^3	6.23×10^{10}	1.28×10^{10}	3.63×10^5	99

^{a}Available experimental data measured in 2-Me-THF in ref 9.

Table 2. Key Geometrical Parameters [including bond lengths (angstroms) and bond angles and dihedral angle (degrees)] of CMAs Obtained from This Work and XRD Experiments

		CAAC−Cu(I)−Cz				CAAC−Au(I)−Cz			
		Cu−C2	Cu−N1	C2−Cu−N1	C1−N1−C2−N2	Au−C2	Au−N1	C2−Au−N1	C1−N1−C2−N2
solution	S_0	1.913	1.874	176.8	5.5	2.039	2.063	175.5	4.6
	S_1	1.887	1.940	175.8	10.4	2.019	2.157	175.2	17.6
	T_1	1.883	1.909	175.4	6.2	2.018	2.135	175.3	8.9
solid	S_0	1.907	1.863	173.7	5.8	2.036	2.048	177.3	−16.2
	S_1	1.896	1.969	172.8	4.7	2.026	2.186	175.6	−19.6
	T_1	1.878	1.900	166.3	6.7	2.012	2.120	172.5	−20.6
crystal[8]	exp.	1.885	1.862	174.3	7.8	1.994	2.027	178.7	−17.7

adiabatic excitation energy as aggregation (see Table S4). The blue-shift emissions of the S_1 state in aggregates for the complexes are from the environmental polarization effect but not the molecular geometry as shown in Table S5.

The calculated rate constants of the excited-state decays are listed in Table 1, in comparison with the available experimental data. First, k_{ISC} and k_{rISC} are found to be most sensitive to environment among all of the rate constants, which increase sharply by several orders of magnitude from solution to solid phase for both copper(I) and gold(I) complexes. The k_{ISC} values of CAAC−Cu(I)−Cz and CAAC−Au(I)−Cz are increased by ≤2 orders of magnitude from 1.52×10^8 and 3.16×10^8 s^{-1} in solution to 5.64×10^{10} and 6.23×10^{10} s^{-1} in aggregates, respectively. Their k_{rISC} values are increased by 4 orders of magnitude from 4.51×10^5 and 4.48×10^6 s^{-1} in solution to 1.74×10^9 and 1.28×10^{10} s^{-1} in aggregates, respectively. Second, the nonradiative rate constants (k_{nr}^S) decrease by 1 order of magnitude upon aggregation for both complexes, which efficiently enhance the luminescence in aggregates. Third, on the basis of the calculated radiative rate constants, we calculate the averaged radiative rate constants by the following equation as $k_{r,avg.} = [k_r^T + k_r^S \exp(-\Delta E_{ST}/k_B T)]/[3 + \exp(-\Delta E_{ST}/k_B T)]$,[33] and we obtain a $k_{r,avg.}$ of 6.58×10^4 s^{-1} in solution for CAAC−Cu(I)−Cz, which is close to the experimental result (3.0×10^5 s^{-1}). The overall TADF quantum efficiencies (ϕ_{TADF}) can be evaluated as[20]

$$\phi_{TADF} = \phi_{PF}[\phi_{ISC}\phi_{rISC}/(1 - \phi_{ISC}\phi_{rISC})] \qquad (6)$$

where $\phi_{ISC} = k_{ISC}/(k_{ISC} + k_r^S + k_{nr}^S)$, $\phi_{rISC} = k_{rISC}/(k_{rISC} + k_r^T + k_{nr}^T)$, and the prompt fluorescence $\phi_{PF} = k_r^S/(k_{ISC} + k_r^S + k_{nr}^S)$. The resultant ϕ_{TADF} of CAAC−Cu(I)−Cz is 72% in solution, which is again in good agreement with the experimentally measured value of 68%,[9] and increases to 98% in aggregates. The ϕ_{TADF} of CAAC−Au(I)−Cz also increases from 92% to 99% upon aggregation (see Table S1). Such a high solid phase luminescence efficiency of the CMAs improves their extraordinary OLED performance.[8,9]

To reveal the inherent structure−property relationship for ISC and rISC, we explore the molecular geometry of the CMAs in the S_0, S_1, and T_1 states in different phases (Table 2). One can see that the optimized ground-state geometries in the solid phase are in good agreement with the experimental crystal data for the two complexes, validating the computational models. Comparing S_1 geometry and T_1 geometry with S_0 geometry, we find that for CAAC−Cu(I)−Cz in solution, the Cu−C2 bond is shortened while the Cu−N1 bond is lengthened upon excitation and the coordination bond angles ∠C2−Cu−N1 between copper and the two ligands are merely changed, while the dihedral angle that corresponds to the rotation of two ligands (∠C1−N1−C2−N2) becomes larger. These findings of geometrical parameters suggest that the excited-state property is mainly controlled by the two ligands rather than the contribution of metal in solution. We find that the S_1 and T_1 minima are in a coplanar orientation. This is quite different from the former reports[12,13] that claim the most stable T_1 minimum has an almost coplanar orientation of the CAAC and Cz π-systems, whereas a perpendicular conformation is found in the global S_1 minimum. To make a direct comparison to these reports, we present the coordinates of the geometrically optimized S_1 and T_1 states obtained from TD/M06 in vacuo in the Supporting Information, and we can testify that our results are qualitatively consistent with those previously reported. In the CAAC−Cu(I)−Cz aggregates, the S_1 optimized geometry experiences quite small changes except for the significant growth of the Cu−N1 bond by 0.106 Å, while the T_1 optimized geometry becomes more bent with angle ∠C2−Cu−N1 decreasing from 173.7° to 166.3°. These results indicate a smaller geometrical relaxation from S_1 to S_0 but a larger geometrical relaxation from S_1 to T_1, upon aggregation. Similar geometrical features are found in S_1 and T_1 in CAAC−Au(I)−Cz from solution to aggregates as seen in Table 2. The role played by the metal atom in the geometrical change in T_1 will be comprehensively investigated in the next section.
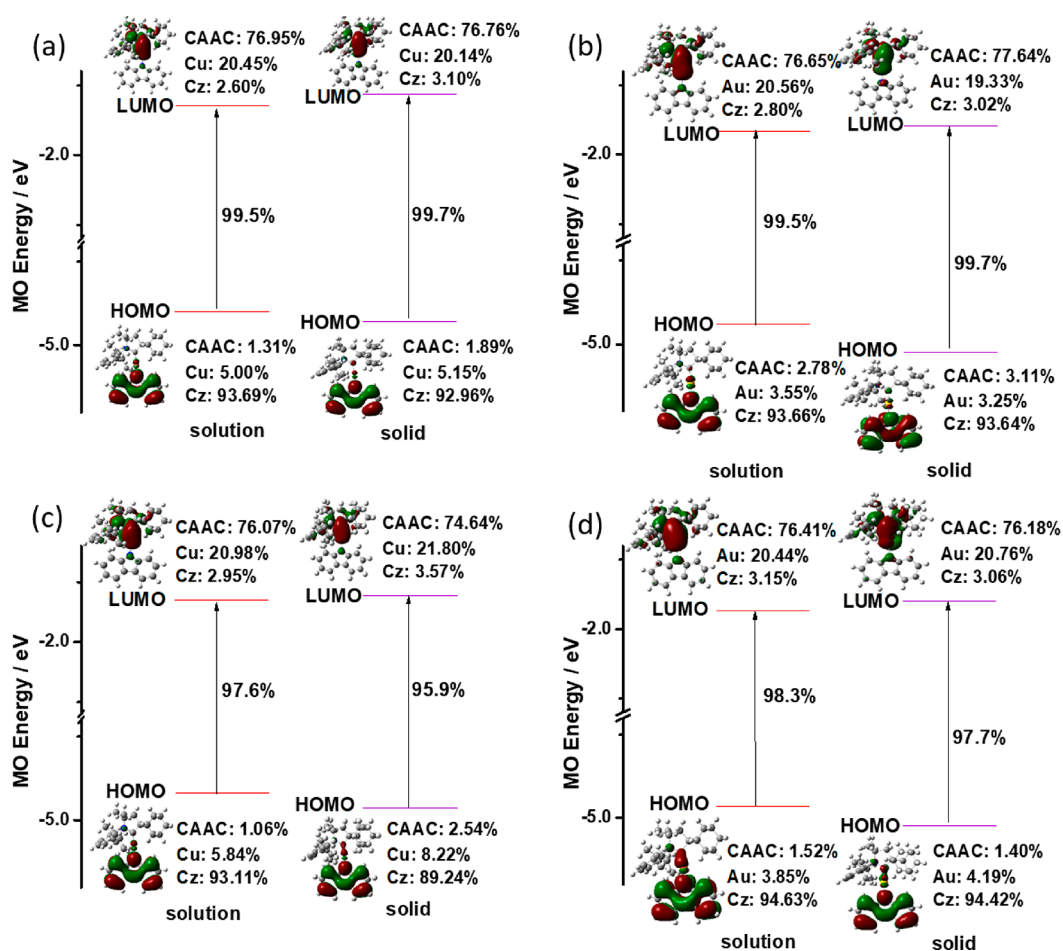
Figure 4. Energy level and composition analysis for the selected frontier orbitals for the S_1 and T_1 states at S_1 geometries and T_1 geometries of (a and c) CAAC−Cu(I)−Cz and (b and d) CAAC−Au(I)−Cz, respectively.

Table 3. Calculated Energy Gaps (ΔE_{ST}) and Activation Energies (ΔG), Spin−Orbit Couplings (ξ), Reorganization Energies ($\lambda_{T_1 \to S_1}$) for the Transition from T_1 to S_1, Reorganization Energies ($\lambda_{S_1 \to T_1}$) for the Transition from S_1 to T_1, and Contributions of the Metal Atom in $\xi_{S_1T_1}$ for CMAs in both Solution and Solid Phase

	ΔE_{ST} (eV)	$\xi_{S_1T_1}$ (cm^{-1})	ξ_{metal} (cm^{-1})	$\lambda_{T_1 \to S_1}$ (cm^{-1})	$\lambda_{S_1 \to T_1}$ (cm^{-1})	ΔG_{ISC} (eV)	ΔG_{RISC} (eV)
			CAAC−Cu(I)−Cz				
solution	0.12 (0.07)[a]	1.84	1.32	151	151	0.14	0.26
solid	0.08	7.35	7.57	530	647	0.01	0.08
			CAAC−Au(I)−Cz				
solution	0.14 (0.11)[b]	0.96	0.97	153	130	0.23	0.37
solid	0.07	8.48	8.62	357	413	0.002	0.07

[a]Vertical ΔE_{ST} calculated in the gas phase in the T_1 optimized geometry at the TDA-PBE0/def2-SVP level.[13] [b]Adiabatic ΔE_{ST} calculated in the gas phase at the DFT/MRCI/def2-TZVP/def-SV(P) level.[12]

On the basis of the optimized geometrical structures of the two complexes in different environments, the electronic structures and properties are then examined. The frontier molecular orbitals (FMOs), their transition properties, and their composition analyses are shown in Figure 4 and Tables S2 and S3. One can see that the highest occupied molecular orbital (HOMO) is mainly localized in the Cz moiety and the metal, while the lowest unoccupied molecular orbital (LUMO) is concentrated on the CAAC moiety and the metal. All excited states of the two complexes in both phases exhibit evident charge transfer (CT) characteristics, including ligand to ligand charge transfer (LLCT) from Cz to CAAC and ligand to metal charge transfer (LMCT) from Cz to metal Cu or Au. Figure 4

and Tables S2 and S3 also show that upon aggregation, the metal component of the FMO is considerably increased at the T_1 optimized geometry while almost unchanged at the S_0 and S_1 optimized geometries, which contributes to the bent structure of T_1 as discussed above. The larger contributions of the Cu or Au atom in the bent T_1 optimized geometry result from the Renner−Teller distortion, which is not uncommon in linear d^{10} coinage complexes.[34] As a result, the transition character from metal to ligand charge transfer (MLCT) becomes more significant, which would improve the SOC due to the heavy atom effect and facilitate the occurrence of ISC/rISC.
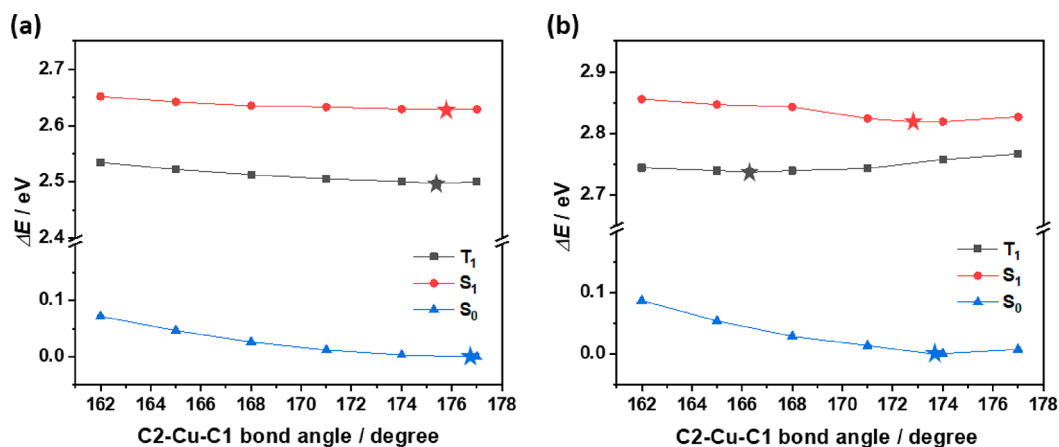
Figure 5. Ground-state and excited S_1- and T_1-state potential energy surfaces (PESs) along the $\angle$C2−Cu−N1 coordinate bond angle of CAAC−Cu(I)−Cz in (a) solution and (b) solid state determined by scanning relaxedly excited-state geometries. The stars correspond to the local minima in the PESs.
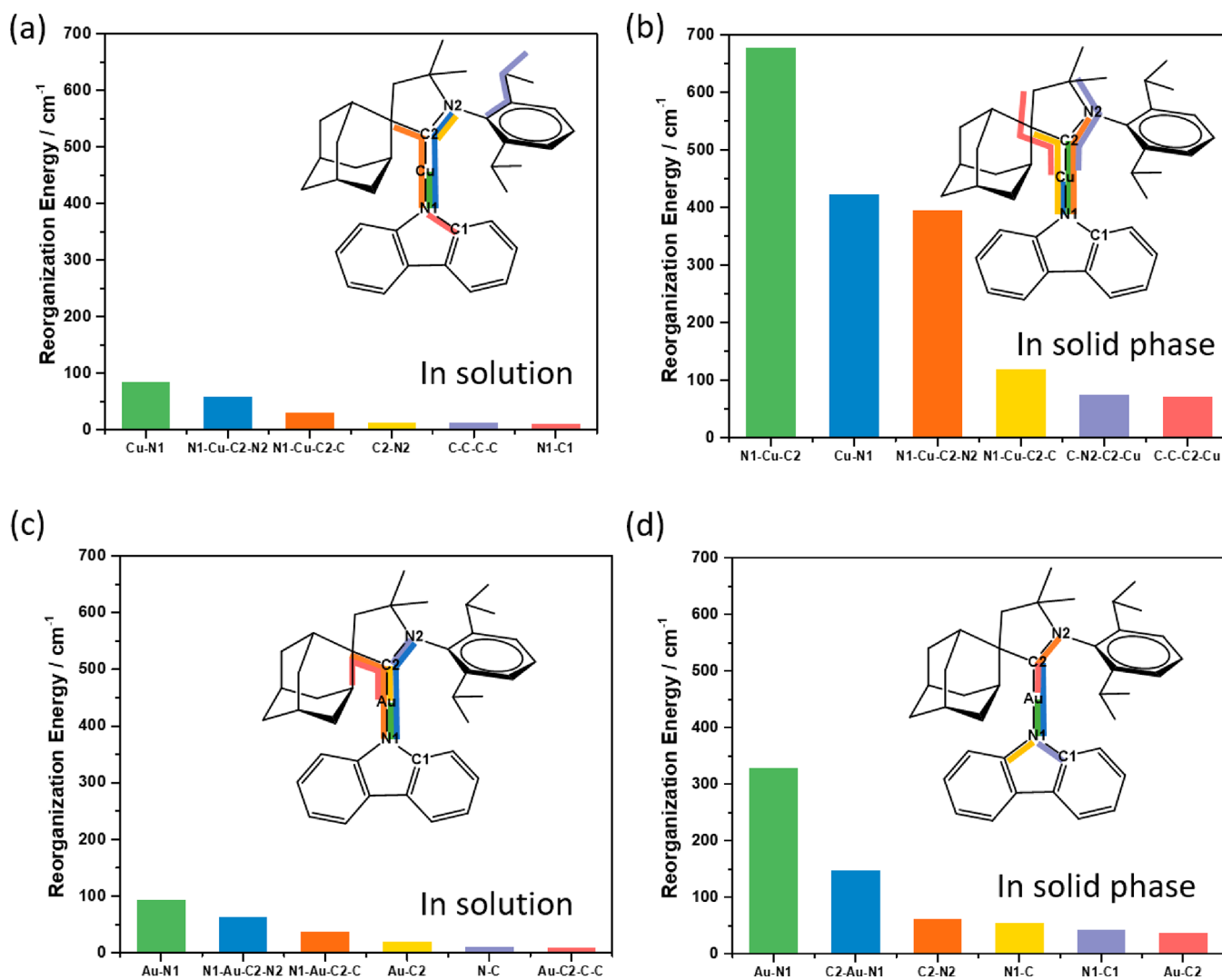

Figure 6. Reorganization energy between S_1 and T_1 states and projections onto the internal coordinates for CAAC−Cu(I)−Cz in (a) solution and (b) solid phase and CAAC−Au(I)−Cz in (c) solution and (d) solid phase.

As mentioned above, the energy gap ΔE_{ST}, the SOC (ξ), and the reorganization energy (λ) are three key factors that determine the rate constants of ISC/rISC.[20,35] The calculated values for these three factors are listed in Table 3, as well as the

activation energy and available reference data.[12,13] The obtained ΔE_{ST} values at the M06/6-31G(d)/LANL2DZ/PCM level in this work are very close to those at the TDA-PBE0/def2-SVP and DFT/MRCI/def2-TZVP/def-SV(P) lev-
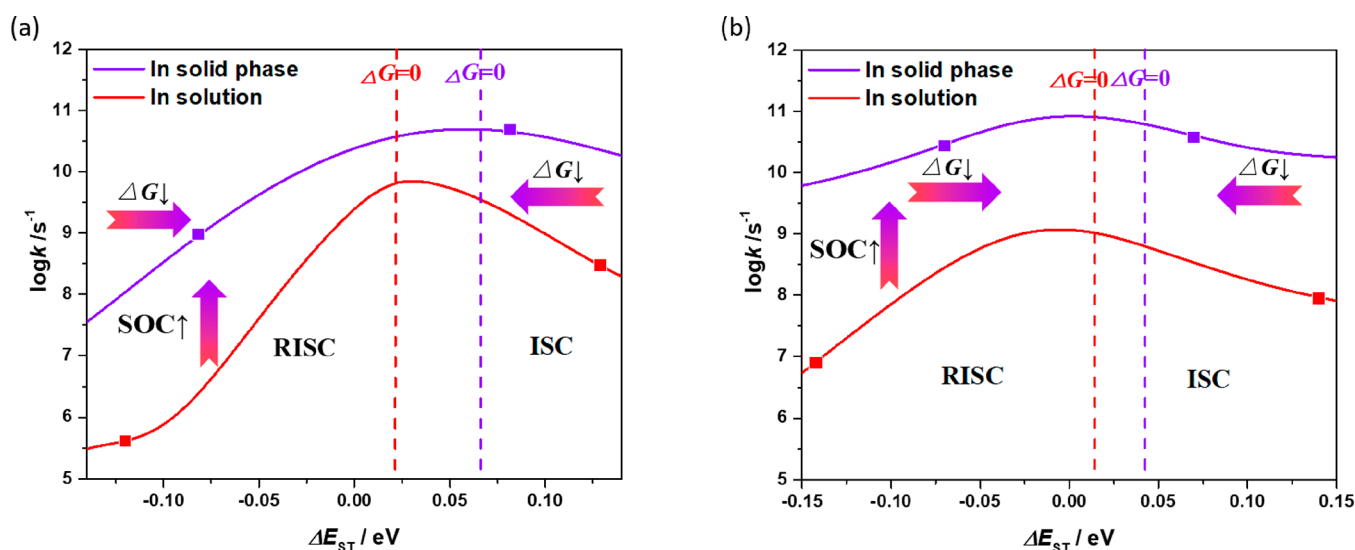
(a)

(b)

Figure 7. Intersystem crossing rate constant as a function of the energy gap of (a) CAAC−Cu(I)−Cz and (b) CAAC−Au(I)−Cz. The points marked with solid squares represent k_{ISC} and k_{rISC}, and the dashed line is the $\Delta G = 0$ when $\Delta E = \lambda$.

els from refs 12 and 13 for the two complexes in solution. As shown in Table 3, the adiabatic ΔE_{ST} is significantly decreased from 0.12 to 0.08 eV for CAAC−Cu(I)−Cz and from 0.14 to 0.07 eV for CAAC−Au(I)−Cz, because the slightly greater increase in the T_1 excitation energy (compared with that of S_1) will therefore decrease the energy gap between S_1 and T_1. Furthermore, the ξ between the S_1 and T_1 states ($\xi_{S_1T_1}$) becomes much stronger upon aggregation, increasing from 1.84 to 7.35 cm^{-1} for CAAC−Cu(I)−Cz and from 0.96 to 8.48 cm^{-1} for CAAC−Au(I)−Cz, which mainly stems from the contribution of the metal atom, i.e., from 1.32 to 7.57 cm^{-1} for CAAC−Cu(I)−Cz and from 0.97 to 8.62 cm^{-1} for CAAC−Au(I)−Cz. To disclose the relationship between the SOC and the coordinate bond angle, we scan the potential energy surface (PES) of T_1 along the $\angle$C2−Cu−N1 angle and calculate the $\xi_{S_1T_1}$ of every point on the PES for CAAC−Cu(I)−Cz, as shown in Figure S1. We found that $\xi_{S_1T_1}$ increases monotonously from 1.04 to 11.1 cm^{-1} with a decrease in $\angle$C2−Cu−N1 from 178° to 150° (Figure S1a) because of the increasing contribution of metal to the transition due to the Renner−Teller distortion (Figure S1b).

To explore the effects of aggregation on the singlet−triplet energy gap and the reorganization energy between the excited singlet and triplet states of the CAAC−Cu(I)−Cz complexes, the relaxed PESs of excited S_1 and T_1 states are scanned along the $\angle$C2−Cu−N1 coordinate bond angle as shown in Figure 5. In solution, the PES is flat, and the local minima of S_1 and T_1 are in the nearly linear conformation, which comes out to be the relatively small reorganization energy between S_1 and T_1. However, the PES becomes much steeper as aggregation, which leads to the fact that the excitation energy increases more considerably in the solid phase for comparable bending angles. Although the adiabatic ΔE_{ST} is decreased in the crystalline phase, the more significant geometrical difference in the S1 and T1 local minima gives rise to a larger reorganization energy between the S_1 and T_1 states. The equilibrium geometry of S_1 in the solid state is also in the quite linear structure, while the triplet minimum energy basin appears at a bent angle of 166.3°.

To unravel the effect of reorganization energy on the (r)ISC rate constant, we first plot the distributions of the reorganization energy between S_0 and S_1 among the normal modes in Figure S4 for the two complexes. As shown in Table S4 and Figure S3, $\lambda_{S_1S_0}$ decreases significantly owing to the limited contribution from the low-frequency mode features from solution to aggregates, resulting in the relatively slow nonradiative decay rate shown in Table 1. On the contrary, $\lambda_{S_1T_1}$ is greatly increased owing to the participation of the low-frequency modes in the solid phase as shown in Table 3 and Figure S5. By projecting $\lambda_{S_1T_1}$ onto the internal coordinates (Figure 6), we find that $\lambda_{S_1T_1}$ mainly comes from the stretching vibration of the Cu−N (Au−N) bond and the bending vibration of coordinate bonds with angles C−Cu−N and C−Au−N. In other words, the Renner−Teller distortions related to metal induce large reorganization energies in the solid phase, which largely accelerate ISC and rISC.

The ISC/rISC rate constant can be analyzed by Marcus theory in terms of activation energy $\Delta G = (-\Delta E_{if} + \lambda)^2/4\lambda$,[20] with the calculated values listed in Table 3. We found that ΔG decreases from 0.14 and 0.26 eV in solution to 0.01 and 0.08 eV, respectively, in aggregates for ISC/rISC for CAAC−Cu(I)−Cz, which accelerates ISC/rISC. To unravel the dependence of the photophysical factors and rate constant on aggregation, we plot k_{ISC} and k_{rISC} as a function of energy gap in Figure 7, and the rate corresponds to k_{ISC} or k_{rISC} when the energy gap is equal to ΔE_{ST}. Figure 7 shows that the rate constant reaches its maximum when $\Delta G = 0$ and $\Delta E = \lambda$, and from solution to aggregates, the increase in SOC and the decrease in ΔG both accelerate ISC/rISC.

It is appropriate to compare this work with our previous studies of the aggregation-induced emission (AIE) phenomena,[36,37] for which the reorganization energy between S_0 and S_1 ($\lambda_{S_1S_0}$) is always largely reduced by aggregation, thus reducing the nonradiative decay rate, because the adiabatic $\Delta E_{S_1S_0}$ is quite large so that decreasing reorganization energy λ implies exponentially decreasing k_{nr}, enhancing luminescence. For ISC/rISC in TADF, $\Delta E_{S_1T_1}$ is typically small, and $\lambda_{S_1T_1}$ is also quite small. Thus, the aggregation-induced increase in $\lambda_{S_1T_1}$
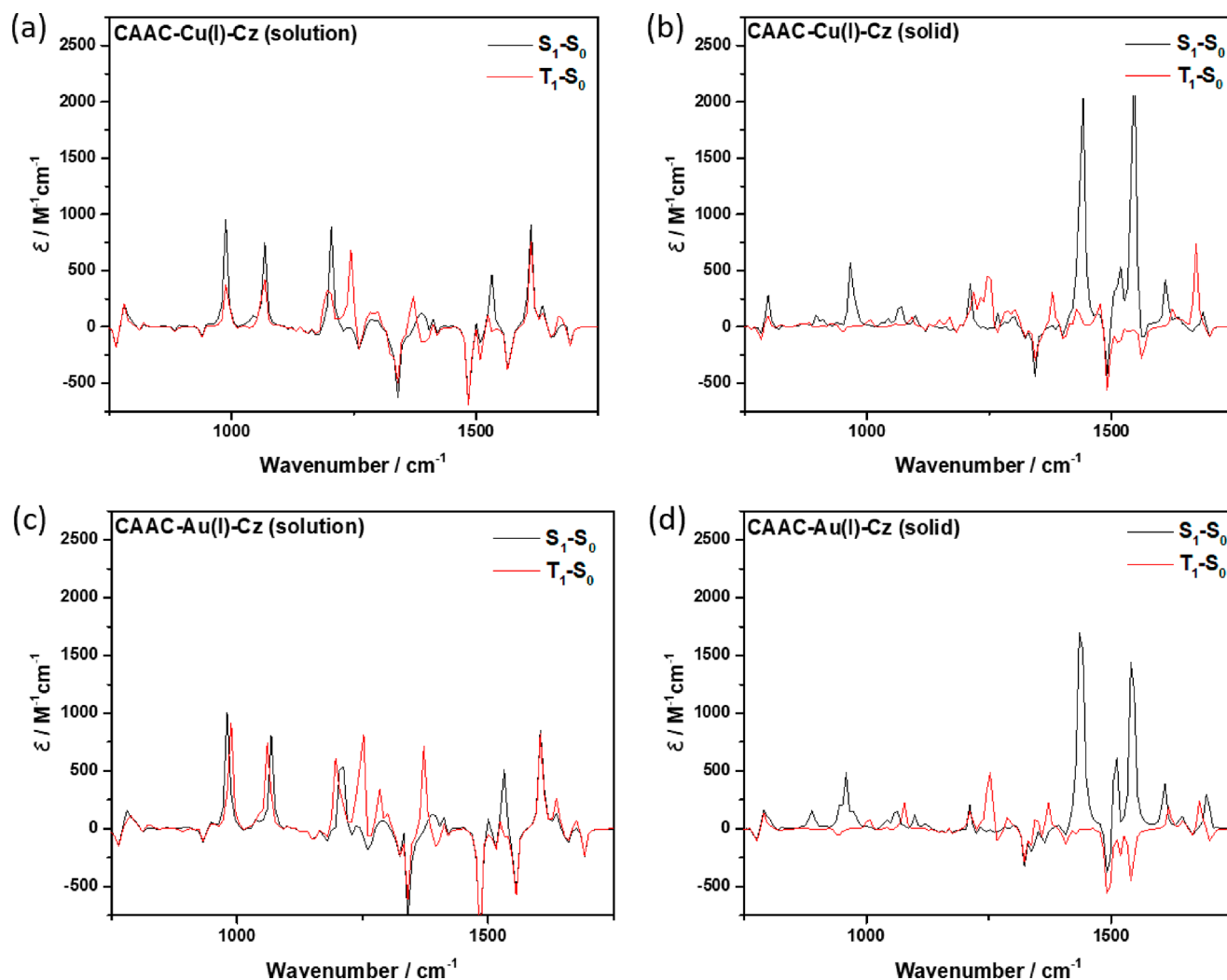
Figure 8. Simulated time-resolved infrared (TR-IR) spectra of CAAC−Cu(I)−Cz in (a) solution and (b) solid phase and CAAC−Au(I)−Cz in (c) solution and (d) solid phase.

leads to enhancement of both ISC and rISC rates, favorable for TADF. We propose using time-resolved infrared (TR-IR) spectra to characterize the deformation between S_1 and T_1 states experimentally.[38,39] We first calculate the IR spectrum of S_0, S_1, and T_1 for the two complexes in different phases (see Figure S6) and take the difference between S_1/T_1 and S_0 to simulate the TR-IR spectra (see Figure 8). We see that there are no obvious deviations in TR-IR spectra for CAAC−Cu(I)−Cz and CAAC−Au(I)−Cz in solution, indicating little deformation between S_1 and T_1. However, the two complexes in the solid phase tend to have significantly different TR-IR spectra for S_1 and T_1 states, indicating a larger $\lambda_{S_1T_1}$ in the aggregate phase.

In summary, the luminescent properties of two-coordinate Cu(I) and Au(I) complexes are comprehensively investigated in solution and solid phase by PCM and QM/MM approaches coupled with TVCF rate formalism. The ISC and rISC rate constants are found to be increased by 2−4 orders of magnitude from solution to solid phase, which leads to the high quantum efficiency of TADF in the solid phase: ϕ_{TADF} increases from 72% to 97% for CAAC−Cu(I)−Cz and from 92% to 99% for CAAC−Au(I)−Cz. Such enhancement of the ISC/rISC rates in CAAC−Cu(I)−Cz upon aggregation mainly stems from the following: (i) increased SOC between S_1 and

T_1 states from 1.84 to 7.18 cm^{-1} due to greater participation of the metal atom of the FMO in aggregates, (ii) increase in the reorganization energy for the $T_1 \rightarrow S_1$ transition from 151 to 647 cm^{-1}, and (iii) decrease in energy gap ΔE_{ST} from 0.12 to 0.08 eV, which decreases activation energy ΔG from 0.14 and 0.26 eV in solution to 0.01 and 0.08 eV, respectively, in aggregates. The Renner−Teller distortion introduces a crooked T_1 optimized geometry with ∠C2−Cu(I)−N1 decreasing to 166.3° in the solid phase, leading to more metal participating in the FMO. The excited S_1- and T_1-state PESs scanned along the ∠C2−Cu−N1 coordinate bond angle become much steeper in the solid state, which gives rise to a relatively larger reorganization energy between S_1 and T_1. Because of a crooked C−Au−N bond angle in aggregates, CAAC−Au(I)−Cz shares similar properties with CAAC−Cu(I)−Cz upon aggregation. Therefore, both ISC and rISC are accelerated in both complexes by the deformation of the C−metal−N coordinate bond leading to strong solid-state TADF. This is quite different from the traditional twisted intramolecular CT (TICT) TADF mechanism that incorporates an extremely small S_1/T_1 energy gap. The proposed mechanism can be verified by the predicted time-resolved infrared spectroscopy. Our comprehensive investigations of the luminescence mechanism of these two representative CMA

complexes would be helpful for the designation of novel highly efficient solid-state luminescent copper/gold complex materials.

■ ASSOCIATED CONTENT

ⓢ Supporting Information

The Supporting Information is available free of charge at https://pubs.acs.org/doi/10.1021/acs.jpclett.1c00020.

Calculated quantum efficiencies, orbital composition, adiabatic energy gaps, vertical excitation energies, SOC constants, reorganization energies, transition dipole moments and infrared spectroscopy for CMAs in solution and solid phase; SOC between S_1 and T_1 states along the increasing bond angle ∠C2−Cu−N1 and selected frontier molecular orbitals and transition properties for CAAC−Cu(I)−Cz; relationships among nonadiabatic couplings, reorganization energies, and normal-mode frequencies; and coordinates of the geometrically optimized S_1 and T_1 states obtained from TD/M06 in vacuo (PDF)

■ AUTHOR INFORMATION

Corresponding Author

Zhigang Shuai − *MOE Key Laboratory of Organic OptoElectronics and Molecular Engineering, Department of Chemistry, Tsinghua University, Beijing 100084, P. R. China;* ⓞ orcid.org/0000-0003-3867-2331; Email: zgshuai@tsinghua.edu.cn

Authors

Shiyun Lin − *MOE Key Laboratory of Organic OptoElectronics and Molecular Engineering, Department of Chemistry, Tsinghua University, Beijing 100084, P. R. China;* ⓞ orcid.org/0000-0002-9394-2149

Qi Ou − *MOE Key Laboratory of Organic OptoElectronics and Molecular Engineering, Department of Chemistry, Tsinghua University, Beijing 100084, P. R. China;* ⓞ orcid.org/0000-0002-6400-7522

Yu Wang − *MOE Key Laboratory of Organic OptoElectronics and Molecular Engineering, Department of Chemistry, Tsinghua University, Beijing 100084, P. R. China*

Qian Peng − *School of Chemical Sciences, University of Chinese Academy of Sciences, Beijing 100049, P. R. China;* ⓞ orcid.org/0000-0001-8975-8413

Complete contact information is available at: https://pubs.acs.org/10.1021/acs.jpclett.1c00020

Notes

The authors declare no competing financial interest.

■ ACKNOWLEDGMENTS

■ REFERENCES

(1) Yersin, H., Ed. Photophysics of Thermally Activated Delayed Fluorescence. In *Highly Efficient OLEDs*; 2018; pp 425−463.

(2) Teng, J.-M.; Wang, Y.-F.; Chen, C.-F. Recent progress of narrowband TADF emitters and their applications in OLEDs. *J. Mater. Chem. C* **2020**, *8* (33), 11340−11353.

(3) Tao, Y.; Yuan, K.; Chen, T.; Xu, P.; Li, H.; Chen, R.; Zheng, C.; Zhang, L.; Huang, W. Thermally Activated Delayed Fluorescence Materials Towards the Breakthrough of Organoelectronics. *Adv. Mater.* **2014**, *26* (47), 7931−7958.

(4) Huang, T.; Jiang, W.; Duan, L. Recent progress in solution processable TADF materials for organic light-emitting diodes. *J. Mater. Chem. C* **2018**, *6* (21), 5577−5596.

(5) Yang, Z.; Mao, Z.; Xie, Z.; Zhang, Y.; Liu, S.; Zhao, J.; Xu, J.; Chi, Z.; Aldred, M. P. Recent advances in organic thermally activated delayed fluorescence materials. *Chem. Soc. Rev.* **2017**, *46* (3), 915−1016.

(6) Wang, H.; Xie, L.; Peng, Q.; Meng, L.; Wang, Y.; Yi, Y.; Wang, P. Novel Thermally Activated Delayed Fluorescence Materials−Thioxanthone Derivatives and Their Applications for Highly Efficient OLEDs. *Adv. Mater.* **2014**, *26* (30), 5198−5204.

(7) Uoyama, H.; Goushi, K.; Shizu, K.; Nomura, H.; Adachi, C. Highly efficient organic light-emitting diodes from delayed fluorescence. *Nature* **2012**, *492* (7428), 234−238.

(8) Di, D. W.; Romanov, A. S.; Yang, L.; Richter, J. M.; Rivett, J. P. H.; Jones, S.; Thomas, T. H.; Abdi Jalebi, M.; Friend, R. H.; Linnolahti, M.; et al. High-performance light-emitting diodes based on carbene-metal-amides. *Science* **2017**, *356* (6334), 159−163.

(9) Hamze, R.; Peltier, J. L.; Sylvinson, D.; Jung, M.; Cardenas, J.; Haiges, R.; Soleilhavoup, M.; Jazzar, R.; Djurovich, P. I.; Bertrand, G.; Thompson, M. E. Eliminating nonradiative decay in Cu(I) emitters: > 99% quantum efficiency and microsecond lifetime. *Science* **2019**, *363* (6427), 601−606.

(10) Romanov, A. S.; Jones, S. T. E.; Gu, Q.; Conaghan, P. J.; Drummond, B. H.; Feng, J.; Chotard, F.; Buizza, L.; Foley, M.; et al. Carbene metal amide photoemitters: tailoring conformationally flexible amides for full color range emissions including white-emitting OLED. *Chemical Science* **2020**, *11* (2), 435−446.

(11) Conaghan, P. J.; Matthews, C. S. B.; Chotard, F.; Jones, S. T. E.; Greenham, N. C.; Bochmann, M.; Credgington, D.; Romanov, A. S. Highly efficient blue organic light-emitting diodes based on carbene-metal-amides. *Nat. Commun.* **2020**, *11* (1), 1758.

(12) Föller, J.; Marian, C. M. Rotationally Assisted Spin-State Inversion in Carbene−Metal−Amides Is an Artifact. *J. Phys. Chem. Lett.* **2017**, *8* (22), 5643−5647.

(13) Taffet, E. J.; Olivier, Y.; Lam, F.; Beljonne, D.; Scholes, G. D. Carbene−Metal−Amide Bond Deformation, Rather Than Ligand Rotation, Drives Delayed Fluorescence. *J. Phys. Chem. Lett.* **2018**, *9* (7), 1620−1626.

(14) Thompson, S.; Eng, J.; Penfold, T. J. The intersystem crossing of a cyclic (alkyl)(amino) carbene gold(i) complex. *J. Chem. Phys.* **2018**, *149* (1), 014304.

(15) Eng, J.; Thompson, S.; Goodwin, H.; Credgington, D.; Penfold, T. J. Competition between the heavy atom effect and vibronic coupling in donor−bridge−acceptor organometallics. *Phys. Chem. Chem. Phys.* **2020**, *22* (8), 4659−4667.

(16) Eng, J.; Penfold, T. J. Understanding and Designing Thermally Activated Delayed Fluorescence Emitters: Beyond the Energy Gap Approximation. *Chem. Rec.* **2020**, *20* (8), 831−856.

(17) Feng, J.; Taffet, E. J.; Reponen, A.-P. M.; Romanov, A. S.; Olivier, Y.; Lemaur, V.; Yang, L.; Linnolahti, M.; Bochmann, M.; Beljonne, D.; et al. Carbene−Metal−Amide Polycrystalline Materials Feature Blue Shifted Energy yet Unchanged Kinetics of Emission. *Chem. Mater.* **2020**, *32* (11), 4743−4753.

(18) Zhang, Q.; Li, B.; Huang, S.; Nomura, H.; Tanaka, H.; Adachi, C. Efficient blue organic light-emitting diodes employing thermally activated delayed fluorescence. *Nat. Photonics* **2014**, *8* (4), 326−332.

(19) de Silva, P.; Kim, C. A.; Zhu, T.; Van Voorhis, T. Extracting Design Principles for Efficient Thermally Activated Delayed Fluorescence (TADF) from a Simple Four-State Model. *Chem. Mater.* **2019**, *31* (17), 6995−7006.

(20) Peng, Q.; Fan, D.; Duan, R.; Yi, Y.; Niu, Y.; Wang, D.; Shuai, Z. Theoretical Study of Conversion and Decay Processes of Excited Triplet and Singlet States in a Thermally Activated Delayed Fluorescence Molecule. *J. Phys. Chem. C* **2017**, *121* (25), 13448−13456.

(21) Shuai, Z.; Peng, Q. Organic light-emitting diodes: theoretical understanding of highly efficient materials and development of computational methodology. *National Science Review* **2017**, *4* (2), 224−239.

(22) Peng, Q.; Niu, Y.; Shi, Q.; Gao, X.; Shuai, Z. Correlation Function Formalism for Triplet Excited State Decay: Combined Spin−Orbit and Nonadiabatic Couplings. *J. Chem. Theory Comput.* **2013**, *9* (2), 1132−1143.

(23) Shuai, Z. Thermal Vibration Correlation Function Formalism for Molecular Excited State Decay Rates. *Chin. J. Chem.* **2020**, *38* (11), 1223−1232.

(24) Gao, Y.-J.; Wang, Z.-R.; Chen, W.-K.; Fang, W.-H.; Cui, G. ONIOM studies on thermally activated delayed fluorescence of copper(I) dimers in crystal. *Chem. Phys.* **2018**, *515*, 692−703.

(25) Cossi, M.; Barone, V.; Cammi, R.; Tomasi, J. Ab initio study of solvated molecules: a new implementation of the polarizable continuum model. *Chem. Phys. Lett.* **1996**, *255* (4), 327−335.

(26) Maseras, F.; Morokuma, K. IMOMM: A new integrated ab initio + molecular mechanics geometry optimization scheme of equilibrium structures and transition states. *J. Comput. Chem.* **1995**, *16* (9), 1170−1179.

(27) Frisch, M.; Trucks, G.; Schlegel, H.; Scuseria, G.; Robb, M.; Cheeseman, J.; Scalmani, G.; Barone, V.; Petersson, G.; Nakatsuji, H. *Gaussian 16*; Gaussian, Inc.: Wallingford, CT, 2016.

(28) Lu, T.; Chen, F. Multiwfn: a multifunctional wavefunction analyzer. *J. Comput. Chem.* **2012**, *33* (5), 580−592.

(29) Abegg, P. W. Ab initio calculation of spin-orbit coupling constants for gaussian lobe and gaussian-type wave functions. *Mol. Phys.* **1975**, *30* (2), 579−596.

(30) Shao, Y.; Gan, Z.; Epifanovsky, E.; Gilbert, A. T.; Wormit, M.; Kussmann, J.; Lange, A. W.; Behn, A.; Deng, J.; et al. Advances in molecular quantum chemistry contained in the Q-Chem 4 program package. *Mol. Phys.* **2015**, *113* (2), 184−215.

(31) Ou, Q.; Subotnik, J. E. Electronic Relaxation in Benzaldehyde Evaluated via TD-DFT and Localized Diabatization: Intersystem Crossings, Conical Intersections, and Phosphorescence. *J. Phys. Chem. C* **2013**, *117* (39), 19839−19849.

(32) Aidas, K.; Angeli, C.; Bak, K. L.; Bakken, V.; Bast, R.; Boman, L.; Christiansen, O.; Cimiraglia, R.; Coriani, S.; Dahle, P.; et al. The Dalton quantum chemistry program system. *WIREs Computational Molecular Science* **2014**, *4* (3), 269−284.

(33) To, W.-P.; Zhou, D.; Tong, G. S. M.; Cheng, G.; Yang, C.; Che, C.-M. Highly Luminescent Pincer Gold(III) Aryl Emitters: Thermally Activated Delayed Fluorescence and Solution-Processed OLEDs. *Angew. Chem., Int. Ed.* **2017**, *56* (45), 14036−14041.

(34) Li, T.-y.; Muthiah Ravinson, D. S.; Haiges, R.; Djurovich, P. I.; Thompson, M. E. Enhancement of the Luminescent Efficiency in Carbene-Au(I)-Aryl Complexes by the Restriction of Renner−Teller Distortion and Bond Rotation. *J. Am. Chem. Soc.* **2020**, *142* (13), 6158−6172.

(35) Wang, Y.; Peng, Q.; Ou, Q.; Lin, S.; Shuai, Z. A novel molecular descriptor for highly efficient (ϕTADF > 90%) transition metal TADF Au(iii) complexes. *J. Mater. Chem. A* **2020**, *8* (36), 18721−18725.

(36) Peng, Q.; Yi, Y.; Shuai, Z.; Shao, J. Toward Quantitative Prediction of Molecular Fluorescence Quantum Efficiency: Role of Duschinsky Rotation. *J. Am. Chem. Soc.* **2007**, *129* (30), 9333−9339.

(37) Zhang, T.; Peng, Q.; Quan, C.; Nie, H.; Niu, Y.; Xie, Y.; Zhao, Z.; Tang, B. Z.; Shuai, Z. Using the isotope effect to probe an aggregation induced emission mechanism: theoretical prediction and experimental validation. *Chemical Science* **2016**, *7* (8), 5573−5580.

(38) Saigo, M.; Miyata, K.; Tanaka, S. i.; Nakanotani, H.; Adachi, C.; Onda, K. Suppression of Structural Change upon S1−T1 Conversion Assists the Thermally Activated Delayed Fluorescence Process in Carbazole-Benzonitrile Derivatives. *J. Phys. Chem. Lett.* **2019**, *10* (10), 2475−2480.

(39) Hosokai, T.; Matsuzaki, H.; Nakanotani, H.; Tokumaru, K.; Tsutsui, T.; Furube, A.; Nasu, K.; Nomura, H.; Yahiro, M.; Adachi, C. Evidence and mechanism of efficient thermally activated delayed fluorescence promoted by delocalized excited states. *Science Advances* **2017**, *3* (5), e1603282.